Soft Matter

ARTICLE TYPE

Cite this: DOI: 10.1039/xxxxxxxxxx

Adhesive elastocapillary force on a cantilever beam†

Tristan Gilet,*[a] Sophie-Marie Gernay,[ab] Lorenzo Aquilante,[b¶] Massimo Mastrangeli,[b‡] and Pierre Lambert [b]

Received Date
Accepted Date

DOI: 10.1039/xxxxxxxxxx

www.rsc.org/journalname

This paper reports an experimental and theoretical investigation of a cantilever beam in contact with an underlying substrate, in the presence of an intervening liquid bridge. The beam is deflected in response to the adhesive capillary forces generated by the liquid. Three main regimes of contact are observed, similarly to other elastocapillary systems already reported in the literature. We measured both the position of the liquid meniscus and the force at the beam clamp in the direction normal to the substrate, as functions of the distance between the beam clamp and the substrate. The resulting force-displacement curve is not monotonic and it exhibits hysteresis in the second regime, that we could attribute to solid-solid friction at the beam tip. In the third regime, the adhesive force measured at the clamp strongly increases as the beam approaches the substrate. A 2-dimensional beam model is proposed to rationalize these measurements. This model involves several non-linearities due to geometrical constraints, and its resolution with a minimum of iterations is not trivial. The model correctly reproduces the force-displacement curve under two conditions: friction is considered in the second regime, and the reaction force applied by the substrate on the beam is distributed in the third regime. These results are discussed in the context of the adhesion of setal tips involved in the terrestrial locomotion of beetles.

1 Introduction

Elastocapillarity, i.e. the deformation of soft or slender structures in response to capillary forces, is omnipresent in the microscopic realm[1]. It can be responsible for the stiction of cantilever structures in microsystems[2]. In Nature, it is involved for instance in the bundling of wet hairs in mammals[3] and oiled bird feathers[4], or the air entrapment in the fur of swimming mammals[5]. It is also a key ingredient for the robust adhesion and walk of many insects on arbitrary solid surfaces[6]. For example, beetles can walk upside-down even on smooth substrates[7] thanks to adhesive pads that consist in arrays of hairs (Fig. 1). The tip of these hairs called setae is wet and very compliant[8]. When a tip comes into close contact with the substrate, the liquid forms a capillary wedge and the resulting adhesion force is sufficient to balance the insect weight. Not only does this strategy work on smooth substrates, it is also very robust to substrates with a wide range of roughness and surface chemistry[6]. The insect does never pre-

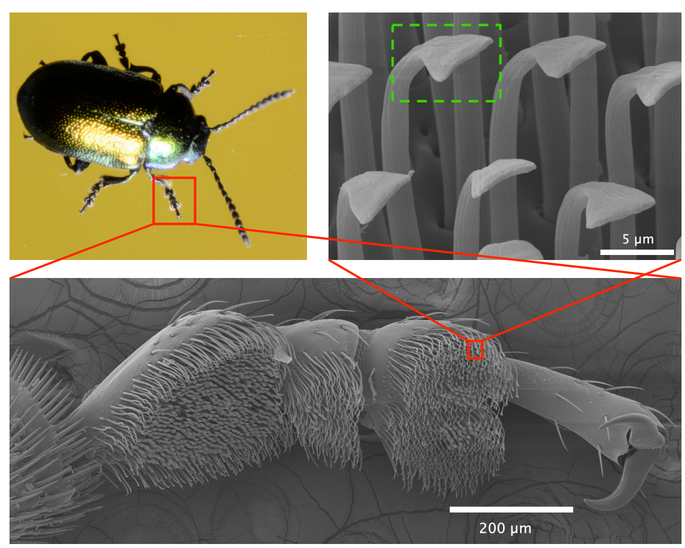

Fig. 1 Male dock beetle *Gastrophysa viridula*, with progressive zoom (red lines) on the adhesive hairy pads of one tarsus, then on individual spaluta-shaped setal tips. The setal tip framed in the green box is the compliant and wet part that provides the required adhesion to the solid surface on which the beetle walks. SEM pictures were taken with the help of Philippe Compère.

[a] Microfluidics Lab, Dept. Aerospace and Mech. Eng., University of Liege, 4000 Liege, Belgium. Tel: 32 4366 9166; E-mail: Tristan.Gilet@uliege.be

[b] TIPS, Université Libre de Bruxelles, 1050 Brussels, Belgium.

† Electronic Supplementary Information (ESI) available: [details of any supplementary information available should be included here]. See DOI: 10.1039/cXsm00000x/

‡ Present address: Electronic Components, Technology and Materials, Dept. Microelectronics, TU Delft, 2628CT Delft, The Netherlands

¶ Present address: Dept. Mech. Eng., Politecnico di Milano, Milan, Italy

cisely control the position of each seta, but it can still attach and detach its hairy pads at will, mostly by rotating these latter and thereby peeling off the setal tips[7]. This biological mechanism suggests a passive and robust way to generate and cancel adhesive forces, which is very appealing for industrial manipulations at the small-scale, including microrobotic pick and place[9].

The elastocapillary equilibrium of a liquid confined by a slender structure has been studied in several configurations: in between a compliant beam and a rigid substrate[8,10], in between two symmetrical beams[11–14], or in between two compliant substrates[15]. The blister test (local peeling of a thin film from a substrate) has also been investigated in presence of capillary forces[16]. In all these studies, focus has been made on the position of the liquid meniscus (both in static and dynamic regimes) and the resulting shape of the deflected slender structure. Three main regimes are recurrently found. In regime 1, both solids do not touch each other but they are instead connected through a liquid bridge. In regime 2, both solids touch each other on a contact line and the bridge turns into a wedge. Finally, in regime 3, both solids apparently touch each other over a finite area. While these universal geometrical features have been systematically reported in previous work, the resulting force applied to the beam has never been measured. This force is nevertheless pivotal to the understanding of insect walking and the development of novel microrobotic handling strategies.

In this paper, we first report measurements of the normal force resulting from the interaction of a compliant millimeter-sized beam with a solid substrate and an intervening liquid wedge. We also characterize the deflection of the beam and the position of the liquid meniscus. This configuration is similar to that investigated in Kwon *et al.*[10], and it is close to that experienced by beetle setal tips[8]. Our experimental setup is described in section 2. The measurements are then presented in section 3. In section 4, we propose an analytical model of regimes 2 and 3 based on Euler-Bernoulli's equation to rationalize our observations. Some key hypotheses commonly made in previous similar models are thereby refuted based on the presented force measurements. In the discussion of section 5, the model is extrapolated to the scale of setal tips. The main results of the paper are summarized in the concluding section 6.

2 Materials and methods

Compliant cantilever beams were produced in SU-8 2050 negative photoresist (MicroChem) by photolithography. A layer of photoresist of approximate thickness 60μm was spin-coated on a flat silicon wafer. It was then exposed to UV light through a mask that defines the horizontal dimensions of the rectangular beams, here with a width $W = 5$mm (the length is defined by the clamping conditions presented hereafter). After development, the beams were lifted from the silicon substrate by gently inserting a sharp blade underneath. They were then hard baked at 200°C with a flat surface placed on top to keep them flat. Finally, each beam was firmly clamped at its basis, so its length beyond the clamp was $L = 15$mm. The clamp orientation in the xz-plane could be adjusted by moving a screwed joint.

The clamp was attached to a home-made vertical force sensor

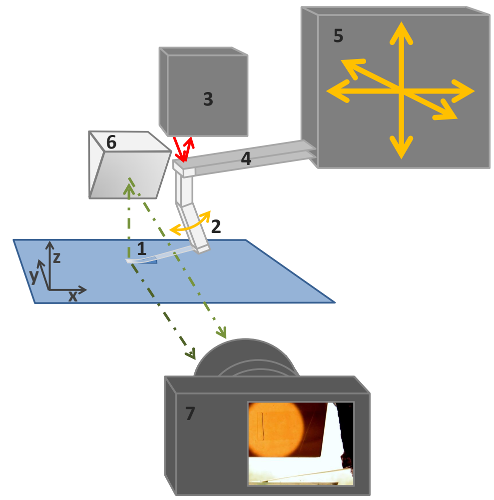

Fig. 2 Experimental setup: The flexible beam to be tested (1) was attached to a clamp allowing rotation in the xz plane (2). The clamp was linked to a force sensor that consisted of a laser displacement sensor (3) and a flexible double cantilever (4). A 3-degree-of-freedom translation stage (5) allowed the full device to be brought at the desired position. A 45° mirror (6) placed at the vertical of the contact allowed the camera (7) to record both lateral and top views simultaneously (see Fig. 3).

based on a double beam (Fig. 2). It consisted in two identical flexible stainless steel beams placed parallel one above another and connected rigidly at both ends. The deflection of this double beam was then forced to be purely vertical[17] and it was recorded with a laser displacement sensor (Keyence LK-G10) offering a theoretical resolution of 10 nm (repeatability 20 nm, linearity 300 nm) on a 2 mm range. The force sensor was calibrated by placing small known weights at its end and measuring the corresponding deflection with the laser sensor. The stiffness of the double beam was $k = 11.5 \pm 0.2$ Nm^{-1}, which allowed to measure a vertical force up to 20mN with a resolution of 0.2μN.

Droplets of silicone oil (DC200 - kinematic viscosity 20 cS) of volume $V_d = 0.16\mu L \pm 10\%$ were dispensed on a plexiglass substrate thanks to a home-made piezoelectric dispenser[18,19]. Several droplets could be dispensed at the same location to reach higher liquid volumes. The assembly made of the SU-8 beam, the clamp and the force sensor was then brought controllably in contact with the liquid, thanks to three automated linear translation stages (M-126 CG1 from Physik Instrumente) with a 2.5μm accuracy and controllable speed. During a typical test, the height of the clamp relative to the underlying substrate was first decreased so the SU-8 beam was forced to touch the substrate, then it was increased again so the beam progressively detached from the substrate.

A high resolution camera (Nikon1 V3 camera, with a $24-85$ mm AF-D NIKKOR lens, resulting resolution 10μm per pixel) placed on the side of the SU-8 beam provided a lateral view of the beam deflection in the xz plane. A typical view from this camera is shown in Fig. 3. The angle of the clamp α_c with the horizontal could be measured on this view, with an accuracy of $\pm 1°$. The distance z_c of the clamp to the substrate could also be

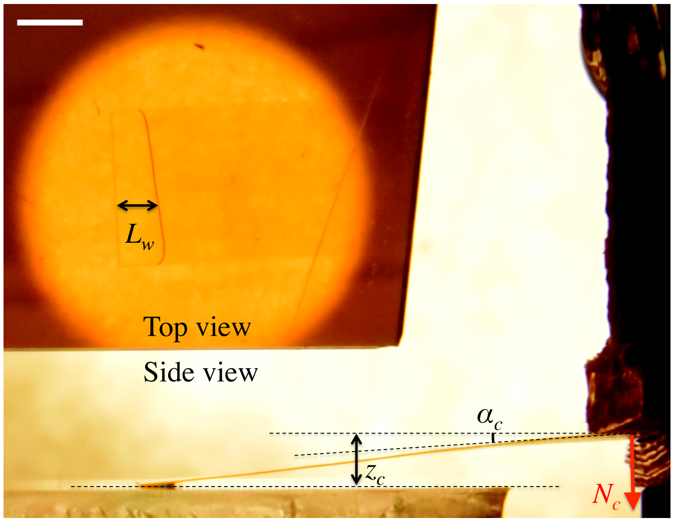

Fig. 3 Side and top view of the SU-8 beam provided by the camera. Several geometrical parameters were measured on the images: the clamping angle α_c, the height of the clamp z_c relative to the substrate and the horizontal extension of the liquid bridge L_w in the x-direction. The vertical force N_c applied by the clamp on the SU-8 beam and measured by the force sensor is also represented (a downward, repulsive force is counted positively). The scale bar is 2mm.

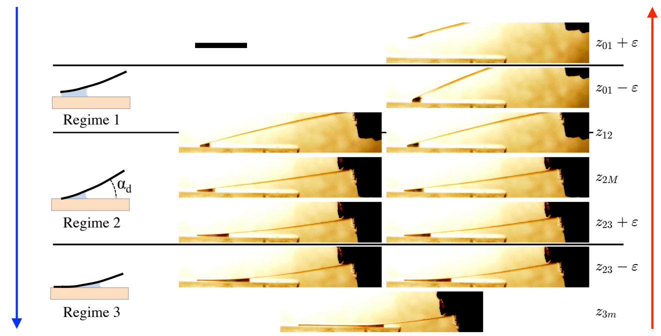

Fig. 4 Characteristic sequence of attachment (left column and blue arrow, from third to seventh line) and detachment (right column and red arrow, from seventh to first line) of the cantilever beam. Each line corresponds to a given clamp height z_c. Attachment starts in regime 2 ($z_{23} < z_c < z_{12}$) and switches to regime 3 ($z_c < z_{23}$), while detachment starts in regime 3 and switches to regime 2, then to regime 1 ($z_{12} < z_c < z_{01}$). The increment ε corresponds to half of the height difference between successive steps, i.e. $\varepsilon \sim 25\mu$m. The liquid volume is $V \simeq 1\mu$L and the clamping angle is $\alpha_c \simeq 12°$. The cantilever length is $L = 15$mm. In regime 2, the beam tip makes an angle α_d with the substrate. The scale bar in the top left corner is 5 mm. The corresponding video is available as ESI.

directly measured. It complemented the more accurate but only relative measurement inferred from the displacements of the vertical translation stage. In addition, a top view of the beam was provided by a 45° mirror positioned above. Since SU-8 is transparent, this top view allowed to see the position of the liquid-air interface in between the beam and the substrate, and to measure its distance L_w to the beam tip.

The compliance of SU-8 beams was measured dynamically from its natural frequency. A load was applied at the beam tip then suddenly removed. The force measured on the clamp showed damped oscillations corresponding to the first mode of bending vibration. The time evolution of these oscillations could be well approximated by $e^{-\beta\omega_0 t}\cos(\omega_0\sqrt{1-\beta^2}t)$, with angular frequency $\omega_0 \simeq 439 \pm 1$rad s^{-1} and damping factor $\beta \simeq 1.3 \pm 0.1\%$. The flexural rigidity B was then calculated as

$$B = \frac{M}{\kappa} = \frac{\omega_0^2 \rho_S L^4 W}{1.8751^4} \simeq 2.9 \times 10^{-7}\text{Nm}^2 \pm 5\% \tag{1}$$

where κ is the local curvature of the beam in response to a local moment M, and $\rho_S \simeq 73 \pm 1$ g m^{-2} is the measured mass per horizontal area of the SU-8 film. The corresponding capillary-bending length was $\ell = \sqrt{B/(\sigma W)} \simeq 54$mm[1], where $\sigma \simeq 20$mNm^{-1} is the surface tension of silicone oil. We define the elastocapillary number

$$\Phi = \frac{L^2}{\ell^2} = \frac{\sigma W L^2}{B} \simeq 0.078 \pm 3\% \tag{2}$$

as a measure of the ability of capillary loads to deform the beam.

The influence of gravity was here assumed negligible. Indeed, the weight of the SU-8 beam was of the order of 54μN, which could be neglected in comparison to the measured levels of adhesive force of the order of 1mN. Moreover, the meniscus height was less than 300μm, which was five times smaller than the capillary length $\sqrt{\sigma/(\rho g)} \simeq 1.5$mm where $\rho \simeq 950$kgm^{-3} is the oil density.

For each beam contact experiment, the clamp position z_c was first lowered down to a distance of the order of $L/10$ from the substrate (attachment phase), then raised up until the liquid bridge breaks up (detachment phase). This vertical motion was performed with discrete steps of 50 μm at a maximum vertical speed of 60 μm s^{-1}. Successive steps were separated by at least 6s in order for the camera to take a snapshot, as well as to allow stabilisation of the SU-8 beam, the liquid bridge and the force sensor. Data from the sensor acquired with a sampling frequency of 100Hz showed small oscillations at about 5Hz (the natural frequency of the double beam), which were removed with a lowpass filter at 3Hz. Several contact experiments were made with different clamping angle $\alpha_c \in [4°, 14°]$ and liquid volume $V \in [0.5, 1]\mu$L (3 to 6 droplets). We define the dimensionless liquid volume Ω, normalized by the beam dimensions:

$$\Omega = \frac{V}{WL^2} \in [4.5, 9] \times 10^{-4}. \tag{3}$$

The liquid was wiped from both the beam and the substrate between each experiment. These latter were then brushed with a metallic ground wire in order to eliminate static charges that could have appeared during wiping.

3 Experimental results

As the clamp height z_c is varied, the beam switches between three different regimes, as already noted by Kwon *et al.*[10]. Figure 4 illustrates these regimes through snapshots taken at 7 characteristic values of z_c. During an attachment / detachment sequence, the beam goes from regime 2 to regime 3, then back to regime 2, and finally to regime 1 until it detaches. The clamp height corresponding to the transition between regime i and regime j is denoted z_{ij}. In regime 1 ($z_{12} < z_c < z_{01}$), the beam does not touch the substrate but there is still a capillary bridge connecting both. In regime 2 ($z_{23} < z_c < z_{12}$), only the beam tip touches the substrate, with a finite angle α_d. There is consequently a reaction force exerted by the substrate on the beam tip in regime 2, that is absent in regime 1. The transition between regimes 1 and 2 ($z_c = z_{12}$) then corresponds to a vanishing reaction. Transition to regime 3 occurs in $z_c = z_{23}$ when the tip inclination α_d vanishes so the tip becomes tangent to the substrate. In regime 3, there is a finite portion of the beam in close contact with the substrate. The lowest position z_{3m} achieved in these experiments is arbitrary.

The distance L_w between the meniscus and the beam tip is reported as a function of the clamp height z_c in Fig. 5a. As the beam is moved towards the substrate, the meniscus is progressively displaced towards the clamp. The variation of L_w with z_c is much more pronounced in regime 3 than in regimes 1 and 2. While the transition between regimes 1 and 2 is smooth, the transition between regimes 2 and 3 (from $z_{23}+\varepsilon$ to $z_{23}-\varepsilon$ and vice versa) is very abrupt and could be assimilated to a discontinuity[10]. The curve $L_w(z_c)$ is fairly independent of the direction of motion (attachment vs. detachment), which suggests that the beam should be in quasi-static equilibrium at each measurement. A very small hysteresis is nevertheless observed around the transition z_{23}.

The vertical force N_c exerted by the beam on the clamp is represented in Fig. 5b. By definition, it is zero when the beam is fully detached from the substrate ($z_c > z_{01}$). In regime 1 ($z_{12} < z_c < z_{01}$), the force is mostly adhesive ($N_c < 0$). A strong and systematic hysteresis appears in regime 2 ($z_{23} < z_c < z_{12}$): the force may become very repulsive ($N_c > 0$) during detachment (with a maximum at position z_{2M}), while it is significantly smaller (and oscillates between adhesion and repulsion) during attachment. This hysteresis disappears in regime 3 ($z_c < z_{23}$), which is characterised by a steep linear increase of the adhesive force ($N_c < 0$) as the beam is brought closer to the substrate. The apparent discontinuity in L_w at the transition z_{23} is not observed for N_c.

Figure 6 shows the force/displacement curve $N_c(z_c)$ for three successive cycles of attachment/detachment in regime 2. Most data points fall on two straight lines, the lower (resp. upper) corresponding to decreasing (resp. increasing) z_c. Each switch of direction is made at an arbitrary clamp height z_c. When the direction is switched, the force toggles to the other straight line. During these transitions, the beam can be stabilised at intermediate positions between both lines. Therefore, this hysteresis cannot be associated to some bistability of the system (that would require switching only at well-defined z_c corresponding to saddle-node bifurcations).

4 Beam model

In this section, we aim at modelling the beam deflection in regimes 2 and 3. In these regimes, the liquid bridge spans the whole width of the beam (Fig. 7 and top view of Fig. 3). On the clamp side, the liquid-air interface can be approximated by a portion of cylinder of radius R that connects to the substrate and to the beam with contact angles θ_s and θ_b, respectively. The cylinder curvature is responsible for a negative Laplace pressure in the liquid bridge $-\sigma/R$, and a corresponding force of the order

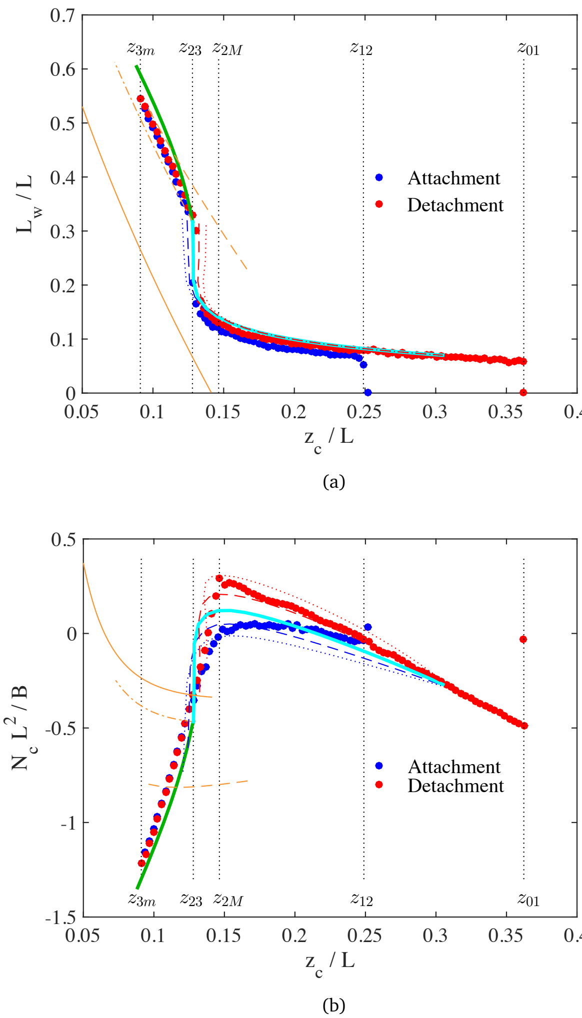

Fig. 5 (a) Wet length L_w from the beam tip to the meniscus (normalised by beam length L), and (b) vertical force at the clamp N_c (normalised by B/L^2), both as functions of clamp height z_c (normalised by beam length L). In both (a) and (b), blue and red dots correspond to experimental measurements during attachment and detachment, respectively. Dotted vertical lines correspond to the snapshots of Fig. 4. The liquid volume is $V \simeq 1\,\mu$L and the clamping angle is $\alpha_c \simeq 12°$. The dotted blue, dashed blue, thick cyan, dashed red and dotted red curves correspond to the model solution of regime 2 with a friction coefficient $\mu = -1$, -0.5, 0, 0.5 and 1, respectively. The thick solid green curve corresponds to the model solution in regime 3, with an adjusted force partition coefficient $m = 0.92$. The dash-dotted (resp. dashed) orange curve is the model solution in regime 3 with a reaction force localized in D and a moment $M_d = 0$ (resp. $M_d = \sqrt{2}/\ell$). All these model curves are calculated with $\alpha_c = 13°$, $\Omega \simeq 9 \times 10^{-4}$ and $\theta_s = \theta_b = 46°$. The solid orange curve corresponds to a dry contact (no capillary force), of a beam again at $\alpha_c = 13°$, with an adhesive energy per unit surface of 0.02 J/m^2 in the solid-solid contact zone (cf. ESI). In (a), the ordinate then corresponds to the length of the solid-solid interface.

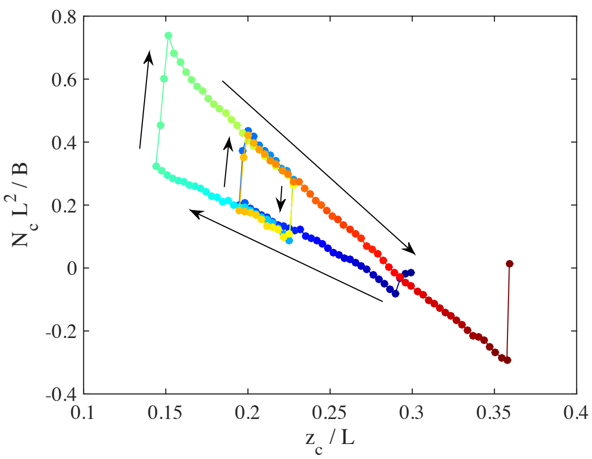

Fig. 6 Vertical force at the clamp N_c (normalised by B/L^2) as functions of clamp distance to the substrate z_c (normalised by beam length L), for three successive cycles of attachment/detachment. Color correspond to the time in the sequence (from dark blue to light blue, green, yellow, orange and finally dark red). Arrows also indicate increasing time. The liquid volume is $V \simeq 0.82\,\mu\mathrm{L}$ and the clamping angle is $\alpha_c \simeq 11.5°$.

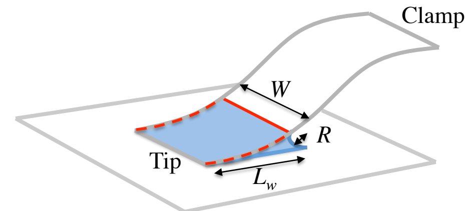

Fig. 7 Schematic 3D view of the beam, substrate and liquid bridge (blue shade) in regimes 2 and 3. Contact lines with the beam are represented in red (solid line on the clamp side, and dashed lines on the lateral sides).

of $\sigma L_w W/R$ that pulls the beam towards the substrate. There is an additional force exerted on the beam by the liquid-air interface at the contact line. The upper bound on this force is σW on the clamp side, and $2\sigma L_w$ on the lateral sides of the beam. The clamp-side contribution cannot be neglected since $R \sim L_w$ in regime 2. By contrast, the lateral-side contribution is negligible with respect to the Laplace force, since the ratio $R/W < 0.1$ in these experiments. Consequently, the liquid bridge can be seen as fully two-dimensional in regimes 2 and 3. This is not true for regime 1, which is therefore not modelled here.

The beam deflection is modelled as described in the schematics of Fig. 8. Points D, W and C represent positions of the right end of the beam/substrate apparent contact zone, the beam/liquid/air contact line and the clamp. In regime 2, D coincides with the beam tip while in regime 3, both are separated by a distance d. The s-axis is tangent to the beam in D, which corresponds to its origin $s = 0$. In regime 2, it makes an angle α_d with the substrate. The beam deflection $y(s)$ is measured perpendicularly to this s-axis.

The beam is loaded with the Laplace pressure σ/R between D and W, and with the capillary force σW at the contact line W. This latter is tangent to the liquid/air interface and makes an angle θ_b with the beam.

Reaction forces and moments applied to the beam from both the clamp and the substrate are defined positive as in Fig. 8. In regime 2, the reaction is localised in D and it comprises both a normal force N_d and a friction force T_d, but no moment ($M_d = 0$) since the beam tip is free to rotate. The direction of the friction force depends on the motion made by the beam tip during the last step of the clamp, which is why hysteresis is observed in the force-displacement curve $N_c(z_c)$ in regime 2. The magnitude of the friction force is unknown a priori, but it should be bounded by the static friction coefficient μ_0. We define the friction coefficient

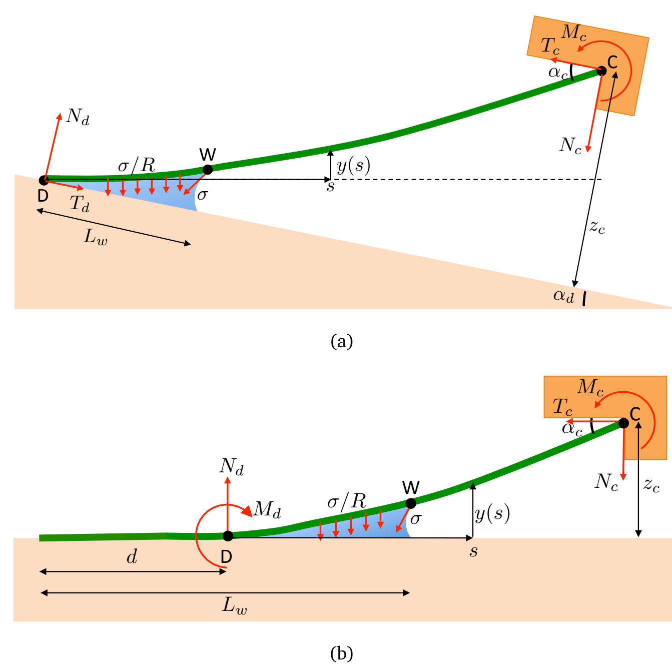

Fig. 8 Two-dimensional schematics of the beam (green), the clamp (orange), the substrate (apricot) and the capillary bridge (blue). (a) Regime 2, represented with an inclination α_d, and (b) regime 3. Forces and moments applied to the beam are represented in red. The main variables of the model are indicated (definition in the text).

$\mu = T_d/N_d \in [-\mu_0, \mu_0]$.

In regime 3, there is a finite region between the beam tip and D where the beam may directly contact the substrate. However, the top view of the liquid bridge obtained through the 45° mirror does not reveal any contact line between the beam, the substrate and the liquid that would suggest some dry contact. We therefore assume that there is always a thin liquid film that lubricates the contact zone between the tip and D, and so cancels friction ($\mu = 0$). In earlier work, it was hypothesized that the existence of such film would correspond to imposing $M_d = 0$ [10,11,20,21]. Here we do not directly make this hypothesis and still consider a moment $M_d \geq 0$ in D (the positive sign is required to prevent the interpenetration of the beam and the substrate). This moment would result from the unknown distribution of reaction forces $f(s)$ between the beam tip and D. The balance of forces and moments on this segment yields

$$\begin{aligned} N_d &= \int_{-d}^{0} f(s)\mathrm{d}s - \frac{\sigma W d}{R} \\ M_d &= \int_{-d}^{0} f(s)(d-s)\mathrm{d}s - \frac{\sigma W d^2}{2R} \\ &= m N_d d - \frac{\sigma W d^2}{2R}(1-2m) \end{aligned}$$

where the parameter

$$m = \frac{\int_{-d}^{0} -s f(s)\mathrm{d}s}{d\int_{-d}^{0} f(s)\mathrm{d}s} \tag{4}$$

is proportional to the first moment of the reaction force distribution. We will also consider the case $M_d = 0$ for the sake of comparison with earlier work.

As the beam is a slender body, it always prefers bending instead of stretching (the stretching stress developed in response to the load is much smaller than the normal bending stress), so hereby the beam length can be assumed constant. We also consider small beam deflections, i.e. $y^2 \ll s^2$ and $\mathrm{d}y/\mathrm{d}s \ll 1$, so the bending curvature can be approximated by $\mathrm{d}^2y/\mathrm{d}s^2$. The deflection $y(s)$ then satisfies the Euler-Bernoulli equation:

$$B\frac{\mathrm{d}^2 y}{\mathrm{d}s^2} = M(s) \tag{5}$$

where $M(s)$ is the moment at abscissa s. An explicit form of $M(s)$ is given in the ESI, as well as a numerical method to efficiently solve this Euler-Bernoulli equation with the aforementioned boundary conditions and geometrical constraints.

4.1 Comparison to experimental results

Several parameters of the model are either completely unknown (m, μ) or known with little accuracy (θ_b, θ_s, Ω), which suggests that their value shall be determined to best fit experimental data. A sensitivity analysis to each parameter is shown in Fig. 9. Increasing the clamping angle α_c mostly shifts both curves $L_w(z_c)$ and $N_c(z_c)$ towards higher z_c. Increasing both contact angles shifts both curves to lower z_c. The very same shift is observed when increasing ℓ (or equivalently decreasing Φ). Indeed, the beam de-

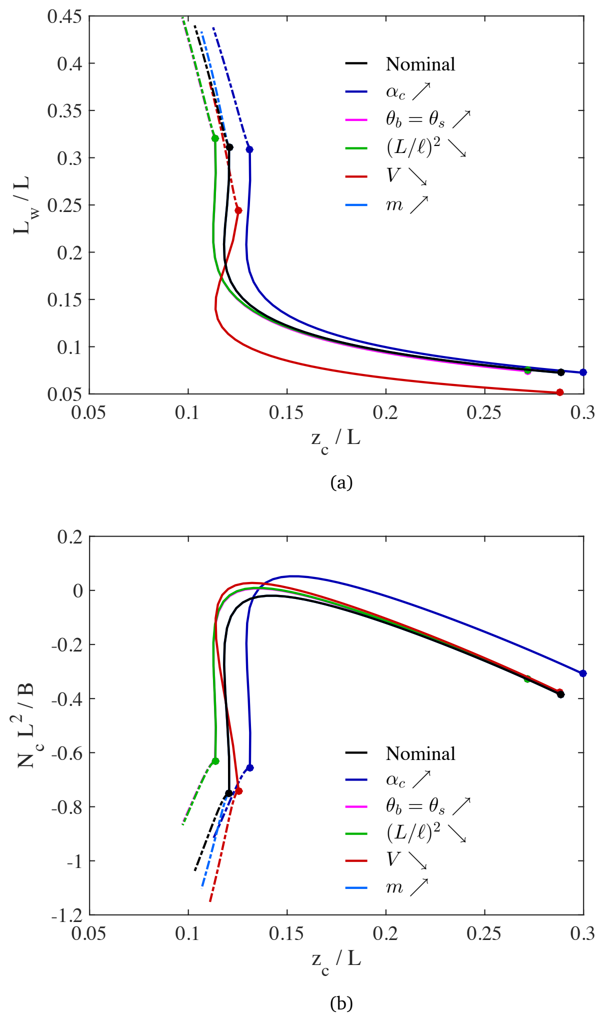

Fig. 9 Variation of model parameters. (a) Wet length L_w from the beam tip to the meniscus (normalised by beam length L), and (b) vertical force at the clamp N_c (normalised by B/L^2), both as functions of clamp height z_c (normalised by beam length L). In both (a) and (b), the black line corresponds to a nominal configuration $\alpha_c = 10°$, $\theta_s = \theta_b = 30°$, $\Omega = 9 \times 10^{-4}$, $\Phi = 0.08$, $m = 0.7$ and $\mu = 0$. Other lines each correspond to one parameter changed at a time: (dark blue) $\alpha_c = 12°$, (magenta) $\theta_s = \theta_b = 45°$, (green) $\Phi = 0.08\sqrt{2/3}$, (red) $\Omega = 4.5 \times 10^{-4}$, and (light blue) $m = 0.8$. Regime 2 (resp. regime 3) is represented with a solid line (resp. dash-dotted line). Magenta and green curves are almost undistinguishable.

flection mostly depends on the ratio $(\cos\theta_s+\cos\theta_b)/\ell^2$, as shown in the ESI. Decreasing the dimensionless volume Ω shifts L_w to lower values, and it makes the $N_c(z_c)$ function more curved in regime 2. Finally, increasing m mostly increases the slope of $N_c(z_c)$ in regime 3.

Experimental data corresponding to eight different contact conditions are then fitted according to the following procedure:

- The model prediction of the transition z_{12} between regimes 1 and 2 is calculated for clamping angles α_c varied within $\pm1.5^\circ$ of the value measured experimentally. The best clamping angle is the one that minimizes the distance between the predicted $N_c(z_{12})$ and the experimental curve $N_c(z_c)$.

- Both $\cos\theta_s=\cos\theta_b$ and Ω are adjusted at the same time, in order to minimize the distance between the predicted and the experimental transition points $L_w(z_{23})$. If the optimum yields $\cos\theta_s>1$, the contact angles are arbitrarily fixed to $\theta_b=\theta_s=5^\circ$ and an increase in Φ is considered instead. The optimal contact angle and the relative correction on volume are $32^\circ\pm23^\circ$ and $-11\%\pm14\%$ respectively (average $\pm$ standard deviation on 8 experiments). For two experiments, a relative increase of less than 6% on Φ was required.

- Parameter m is adjusted to match the average experimental value of $\mathrm{d}N_c/\mathrm{d}z_c$ in regime 3. Its optimal value is 0.76 ± 0.09.

Finally, several values of the friction coefficient are considered in regime 2. These experimental data and the corresponding fitted parameters are available as ESI.

The adjusted solution of the model is represented against experimental data in Fig. 5. The agreement is qualitatively excellent in all regimes. The model always correctly predicts some friction-dependent repulsion ($N_c>0$) increasing with decreasing z_c in regime 2, some friction-independent adhesion ($N_c<0$) increasing with decreasing z_c in regime 3, a steep increase of the wet length L_w with decreasing z_c in regime 3, and a sharp transition between regimes 2 and 3 that looks like a discontinuity. Nevertheless, the quantitative agreement is far from perfect, despite the fitting of model parameters. Some of the discrepancy could be attributed to the fact that contact angles θ_b and θ_s, friction coefficient μ and parameter m could be significantly varying during a single contact experiment.

According to the model, the attachment (resp. detachment) curve of Fig. 5 corresponds to $\mu<0$ (resp. $\mu>0$), and so to a friction force T_d directed away from (resp. toward) the clamp. This is counter-intuitive since the beam tip naturally moves away from (resp. toward) the clamp for decreasing z_c (resp. increasing z_c) as it cannot significantly stretch. This paradox comes from an experimental artifact: at each increment of the z_c position, the clamp experiences a slight overshoot, and so does the beam tip. The force measurement is performed when the beam is back to its new equilibrium position. Since the friction force is opposed to the last motion before equilibrium, it is therefore pointing in the same direction as the natural motion of the tip.

4.2 Alternative hypotheses

The model of regime 3 is based on the hypothesis of a distributed reaction force through the parameter m. In the previous models of elastocapillary adhesion, the reaction force was assumed to be localized in D, and the moment was either $M_d=0$[10–14] or $M_d=\sqrt{2}/\ell$[22,23]. The corresponding solutions to the Euler-Bernoulli equation are derived in the ESI, and are represented in Fig. 5. Although such alternative hypotheses on M_d give reasonably accurate predictions of $L_w(z_c)$ as already noted in several previous works[10,11], they completely fail at predicting the increased adhesion $-N_c$ with decreasing z_c in regime 3.

We also calculated the deflection of the beam in the case of a dry contact (with no liquid bridge) and a net adhesive surface energy for the solid-solid interface between the beam and the substrate (cf. ESI). The length of the solid-solid contact area as well as the net adhesive force N_c are represented in Fig. 5. On the one hand, the length of this solid-solid dry contact is again fairly close to that obtained experimentally for wet beams (though with an expected shift corresponding to the distance between D and W in Fig. 8, which does not exist in a dry contact). On the other hand, the adhesive force again decreases as the clamping point approaches the substrate, which again contrasts with the measurements in regime 3. The strong adhesive force measured when the beam is close to the substrate is therefore a specificity of elastocapillary adhesion.

5 Discussion on the adhesion mechanism of setal tips

The SU-8 beams could be seen as a model of the setal tips of e.g., dock beetles, scaled-up 1000 times. To ensure similitude, the elastocapillary number Φ, the dimensionless volume of liquid Ω, and the angles α_c, θ_s and θ_b should be the same in both systems (we also have first to assume that during the bettle's walk, the setal tips are mostly subjected to the same quasi-static bending as the SU-8 beams). The setal tips of dock beetles (Fig. 1) have a width $W_s\simeq5$ µm and a length $L_s\simeq7$µm. Their flexural rigidity[8] is of the order of $2\times10^{-18}\mathrm{Nm}^2$ (The stalk is several orders of magnitude more rigid[24]). If the surface tension is assumed the same as for most oils, i.e. $\sigma\simeq0.02\mathrm{Nm}^{-1}$, the capillary-bending length is $\ell\sim4.5$µm and the elastocapillary number is $\Phi\sim2.4$ (the elastocapillary number of our SU-8 beams is about 0.078). Setal tips are therefore significantly more compliant than the present SU-8 beams, and they are prone to larger deformations under capillary loads. The volume of liquid under setal tips is of the order of 0.3fl per tip[8], which corresponds to $\Omega\sim1.2\times10^{-3}$. The 1µl dispensed under the SU-8 beams corresponds to $\Omega\simeq9\times10^{-4}$, so similitude is approximately achieved in terms of liquid volume. The clamping angle has never been characterized for setal tips. Nevertheless, it certainly varies as the beetle walks since both attachment and detachment of the tarsal segments are mostly performed by peeling[7]. Data on the contact angle of the beetle secretion with various substrates are scarce[6]; angles $\theta_s\sim10^\circ$ have been reported on mica[25]. We may assume that the beetle cuticle itself would be similarly wet by the secretion. Consequently, we may assume that $\cos\theta_s\simeq\cos\theta_b\simeq1$ for the beetle.

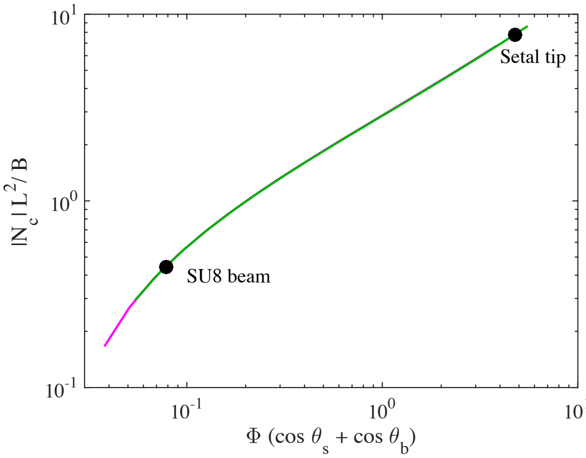

Fig. 10 Normalized adhesion force $|N_c|L^2/B$ in $z = z_{23}$, as a function of $\Phi(\cos\theta_s + \cos\theta_b)$, according to the beam model of Section 4. The clamping angle is $\alpha_c = 10°$ and the normalized volume is $\Omega = 9\times10^{-4}$. The green curve corresponds to $\theta_s = \theta_b = \pi/6$ while the pink curve corresponds to $\theta_s = \pi/3$ and $\theta_b = \pi/4$.

Figure 10 shows the normalized adhesion force $|N_c|L^2/B$ at the onset of regime 3 (i.e., in z_{23}), as a function of the group $\Phi(\cos\theta_s + \cos\theta_b)$. In this representation, data corresponding to different sets of contact angles (θ_s, θ_b) fall on a same curve, as already noted in Fig. 9. The normalized adhesion force increases with increasing $\Phi(\cos\theta_s + \cos\theta_b)$. However, the dimensional adhesion force $|N_c| = \sigma W(|N_c|L^2/B)/\Phi$ decreases with increasing Φ, since $|N_c|L^2/B$ is less than proportional to Φ (Fig. 10). For setal tips, $\Phi(\cos\theta_s + \cos\theta_b) \sim 5$, which corresponds to $|N_c|L^2/B \sim 8$ and so the adhesion force at the onset of regime 3 is $|N_c| \sim 0.33\mu$N. Figure 5 suggests that the adhesion can increase by at least a factor of 2 as the clamp height z is decreased in regime 3. This order of magnitude corresponds very well to the normal pull-off force measurements on single setae of dock beetles[26]. A more realistic model of a setal tip should include variations of B with s induced by its three-dimensional geometry (both width W and thickness vary with s) and by the heterogeneous material composition of the setal tip[8]. These variations $B(s)$ for setal tips have not been measured *in vivo* yet. Other forces (e.g., van der Waals forces or lubrication) may also have to be considered to faithfully explain the mechanical behavior of setal tips[6]. Finally, the setal tip is here modeled as clamped to a rigid and fixed setal stalk, which is likely inaccurate. Indeed, the transition from the setal stalk to the setal tip is rather continuous (Fig. 1) so part of the stalk might be deformed at the same time as the setal tip, which would in turn modify the clamping angle.

In addition to providing sufficient adhesion when needed, setal tips also have to be detached effortlessly. The friction-induced hysteresis observed in regime 2 would be advantageous for this purpose, as it yields a repulsive normal force only when the friction force at the tip is oriented toward the clamp. This would provide some rationale for why beetles[7] and flies[27] often perform proximal pulls to attach their hairy pads and distal pushes to detach them.

6 Conclusion

In this paper, we have considered the elastocapillary equilibrium of a millimeter-sized slender cantilever beam in partial contact with a solid substrate, with some intervening liquid. We proposed this configuration as a model of the setal tips of hairy adhesive pads in beetles[8]. The beam is deflected in response to the reaction force and torque on the substrate, as well as to the capillary forces from the liquid wedge. Similar configurations were already investigated experimentally and theoretically, but only with an emphasis on the position of the liquid meniscus L_w as a function of the distance of the clamp to the substrate z_c[10]. In addition, we have here measured the force N_c exerted by the beam on the clamp in the direction normal to the substrate. The force-displacement curve shows non-trivial behaviours, including hysteresis and variations of slope sign. We have then revisited the theoretical model based on Euler-Bernoulli's differential equation initially proposed in Kwon *et al.*[10] and Gernay *et al.*[8]. We have proposed an original method to solve the corresponding non-linear boundary problem at minimal computational cost, with only one main bisection loop.

The three regimes often encountered in elastocapillary systems (namely no contact, point contact and extended contact area) have been observed here. The $L_w(z_c)$ curve is very similar to that of Kwon *et al.*[10]. In particular, it shows some apparent discontinuity at the transition z_{23} between regimes 2 and 3, that is reminiscent of systems with two coexisting stable states[14]. However, no such discontinuity is seen in normal force measurements $N_c(z_c)$.

Some hysteresis is observed in the whole regime 2. The force N_c is always more repulsive during detachment than during attachment. The model confirmed that this hysteresis is not due to bistability, but rather to the direction-dependent friction force exerted by the substrate on the beam tip. The resulting force at the clamp N_c is slightly adhesive if the beam tip slides toward the clamp, but it is strongly repulsive when the tip moves away from the clamp. This friction-induced hysteresis is almost absent in regime 2 on $L_w(z_c)$ curves, which explains why it has not been identified in earlier work[10]. Contact angle hysteresis may also participate to the observed difference between attachment and detachment curves. During attachment, the contact line advances, which yields a larger contact angle than during detachment. According to Fig. 9b, this larger contact angle would correspond to a smaller N_c, consistently with experiments. Nevertheless, the effect of contact angle hysteresis is much less pronounced than that of friction, and it cannot alone explain the observed direction dependence in regime 2.

The hysteresis completely disappears in regime 3, which suggests that both the effects of the friction force and contact angle hysteresis become negligible. The strongly reduced friction could be due to some lubrication of the apparent contact area by the intervening liquid film. Many previous authors argued that in the presence of such film, the reaction force could be considered as being concentrated at the extremity of the contact zone (point D), and the moment M_d at this location should be zero. Conversely, the absence of such film would yield a finite and constant M_d proportional to the square root of the solid-solid adhesion energy. While the model correctly reproduce the measured $L_w(z_c)$ with such hypothesis of constant M_d, it completely fails at predicting the observed strong linear increase of adhesion as z_c decreases. We therefore considered a finite and non-constant moment M_d that would result from both a distribution of the reaction force over the contact area and the presence of Laplace pressure in the liquid film. We could expect that such distribution depends on the roughness of the substrate, and it is therefore unknown. However, only the first moment of this distribution does matter for bending deformations. With an appropriate fit of this scalar parameter, the model correctly reproduces the measured adhesion N_c as a function of z_c. All other modelling attempts not considering this contact distribution failed at correctly capturing force variations in regime 3.

In conclusion, this work provided a renewed picture of the elastocapillary equilibrium of a wet beam in contact with a substrate, in the light of normal force vs. displacement measurements. Most notably, these measurements revealed the importance of friction in regime 2, and contact distribution in regime 3. It is hoped that these results will help to better understand the adhesion mechanisms of insect hairy pads, and that they will stimulate attempts to build improved biomimicked microrobotic pick-and-place systems.

References

1 J. Bico, E. Reyssat and B. Roman, *Annu. Rev. Fluid Mech.*, 2018, **50**, 629–659.

2 W. M. van Spengen, R. Puers and I. de Wolf, *J. Micromech. Microeng.*, 2002, **12**, 702–713.

3 J. Bico, B. Roman, L. Moulin and A. Boudaoud, *Nature*, 2004, **432**, 690.

4 C. Duprat, S. Protiere, A. Y. Beebe and H. A. Stone, *Nature*, 2012, **482**, 510–513.

5 A. Nasto, M. Regli, P.-T. Brun, J. Alvarado, C. Clanet and A. E. Hosoi, *Phys. Rev. Fluids*, 2016, **1**, 033905.

6 T. Gilet, L. Heepe, P. Lambert, P. Compère and S. N. Gorb, *Curr. Opin. Insect Sci.*, 2018, **30**, 19–25.

7 S. M. Gernay, S. Labousse, P. Lambert, P. Compère and T. Gilet, *J. R. Soc. Interface*, 2017, **14**, 20170493.

8 S. M. Gernay, W. Federle, P. Lambert and T. Gilet, *J. R. Soc. Interface*, 2016, **13**, 20160371.

9 P. Lambert, *Capillary Forces in Microassembly*, Springer, 2007.

10 H.-M. Kwon, H.-Y. Kim, J. Puëll and L. Mahadevan, *J. Appl. Phys.*, 2008, **103**, 093519.

11 H.-Y. Kim and L. Mahadevan, *J. Fluid Mech.*, 2006, **548**, 141–150.

12 J. M. Aristoff, C. Duprat and H. A. Stone, *Int. J. Non-Linear Mech.*, 2011, **46**, 648–656.

13 C. Duprat, J. M. Aristoff and H. A. Stone, *J. Fluid Mech.*, 2011, **679**, 641–654.

14 M. Taroni and D. Vella, *J. Fluid Mech.*, 2012, **712**, 273–294.

15 J. S. Wexler, T. M. Heard and H. A. Stone, *Phys. Rev. Lett.*, 2014, **112**, 066102.

16 J. Chopin, D. Vella and A. Boudaoud, *Proc. R. Soc. A*, 2008, **464**, 2887–2906.

17 F. Cosandier, S. Henein, M. Richard and L. Rubbert, *The art of flexure mechanism design*, EPFL press distributed by CRC press, Boca Raton, 1st edn, 2017.

18 D. Terwagne, F. Ludewig, N. Vandewalle and S. Dorbolo, *Phys. Fluids*, 2013, **25**, 122101.

19 D. M. Harris, T. Liu and J. W. M. Bush, *Exp. Fluids*, 2015, **56**, 83.

20 J. W. Obreimoff, *Proc. R. Soc. A*, 1930, **127**, 290–297.

21 R. A. Sauer, *J. Adhesion*, 2011, **87**, 624–643.

22 C. Majidi and G. G. Adams, *Proc. R. Soc. A*, 2009, **465**, 2217–2230.

23 B. Roman and J. Bico, *J. Phys.: Condens. Matter*, 2010, **22**, 493101.

24 H. Peisker, J. Michels and S. N. Gorb, *Nat. Comm.*, 2013, **4**, 1661.

25 L. Heepe, J. O. Wolff and S. N. Gorb, *Beilstein J. Nanotechnol.*, 2016, **7**, 1322–1329.

26 J. M. R. Bullock and W. Federle, *Naturwissenschaften*, 2011, **98**, 381–387.

27 S. Niederegger and S. N. Gorb, *J. Insect Physiol.*, 2003, **49**, 611–620.